Nanoscale Tailoring of the Polarization Properties of Dilute-Nitride Semiconductors via H-Assisted Strain Engineering

Marco Felici,[1,*] Simone Birindelli,[1] Rinaldo Trotta,[2] Marco Francardi,[3] Annamaria Gerardino,[3] Andrea Notargiacomo,[3] Silvia Rubini,[4] Faustino Martelli,[4,5] Mario Capizzi,[1] and Antonio Polimeni[1]

[1]*Dipartimento di Fisica and CNISM, Sapienza Università di Roma, Piazzale Aldo Moro 2, 00185 Roma, Italy*
[2]*Institute of Semiconductor and Solid State Physics, Johannes Kepler University Linz, Altenbergerstrasse 69, A-4040 Linz, Austria*
[3]*CNR-Istituto di Fotonica e Nanotecnologie, Via Cineto Romano 42, 00156 Roma, Italy*
[4]*TASC-IOM-CNR, Area Science Park, Strada Statale 14, Km 163.5, 34149 Trieste, Italy*
[5]*IMM-CNR, Via del Fosso del Cavaliere 100, 00133 Roma, Italy*

(Received 3 August 2014; revised manuscript received 20 November 2014; published 22 December 2014)

In dilute-nitride semiconductors, the possibility to selectively passivate N atoms by spatially controlled hydrogen irradiation allows for tailoring the effective N concentration of the host—and, therefore, its electronic and structural properties—with a precision of a few nanometers. In the present work, this technique is applied to the realization of ordered arrays of $GaAs_{1-x}N_x/GaAs_{1-x}N_x{:}H$ wires oriented at different angles with respect to the crystallographic axes of the material. The creation of a strongly anisotropic strain field in the plane of the sample, due to the lattice expansion of the fully hydrogenated regions surrounding the $GaAs_{1-x}N_x$ wires, is directly responsible for the peculiar polarization properties observed for the wire emission. Temperature-dependent polarization-resolved microphotoluminescence measurements, indeed, reveal a nontrivial dependence of the degree of linear polarization on the wire orientation, with maxima for wires parallel to the [110] and $[1\bar{1}0]$ directions and a pronounced minimum for wires oriented along the [100] axis. In addition, the polarization direction is found to be precisely perpendicular to the wire when the latter is oriented along high-symmetry crystal directions, whereas significant deviations from a perfect orthogonality are measured for all other wire orientations. These findings, which are well reproduced by a theoretical model based on finite-element calculations of the strain profile of our $GaAs_{1-x}N_x/GaAs_{1-x}N_x{:}H$ heterostructures, demonstrate our ability to control the polarization properties of dilute-nitride micro- and nanostructures via H-assisted strain engineering. This additional degree of freedom may prove very useful in the design and optimization of innovative photonic structures relying on the integration of dilute-nitride-based light emitters with photonic crystal microcavities.

DOI: 10.1103/PhysRevApplied.2.064007

I. INTRODUCTION

In modern-day semiconductor science and technology, the coexistence of materials with different lattice parameters and/or elastic properties has become commonplace, triggering extensive investigations on the effects of elastic strain on the optical, electrical, and structural properties of semiconductors [1–4]. Eventually, these studies have resulted in the development of microfabrication protocols that allow for manipulating and improving the performance of optoelectronic devices through fine adjustments of the local strain profile. This practice, generally known as strain engineering, was instrumental to the huge performance boost achieved in the last decade by CMOS-based logic technologies, the founding element of current mainstream microprocessors [4–6]. However, strain-engineering methods—and strain-related effects, in general—play a very important role in many other areas of semiconductor research, both at the level of fundamental studies and within fields that are closer to generating mass-market applications. For instance, the release of strain following epitaxial deposition of a thin semiconductor film on a highly mismatched substrate is the driving force behind the nucleation of Stranski-Krastanow quantum dots (QDs) [7,8], which are widely employed as single quantum emitters in advanced nanophotonics devices [9–12] and actively investigated for their potential use in the realization of low-threshold, temperature-insensitive QD lasers [13,14]. Also, the strain-related nanoscale deformation (approximately 0.1 nm) associated with the deposition of Ge QDs on a Si substrate was recently demonstrated [15]—as theoretically predicted in 2006 by Sawada *et al.* [16]—to be sufficient to induce a macroscopic splitting (approximately 0.2 mm) in an x-ray beam transmitted through the material, paving the way to the realization of innovative optical elements useful for applications in x-ray pump-and-probe experiments and in x-ray interferometry.

*marco.felici@roma1.infn.it

 © 2014 American Physical Society

In the following, we discuss how dilute-nitride semiconductors—III-V alloys containing less than a few percent of N atoms (≤5%) [17]—provide the ideal environment for the development of a new, very promising method of strain engineering. As thoroughly documented in the literature [17], the incorporation of a small percentage of N atoms in III-V materials such as GaAs and GaP leads to a wide variety of striking effects: These include, just to give a few examples, a large and unexpected redshift of the energy gap [17–19]; a striking nonmonotonic dependence of the electron effective mass on N composition [20] and hydrostatic pressure [21]; and the introduction of a series of very efficient radiative centers [22–24], which have recently shown the ability to emit single photons [25]. Following irradiation with H^+ ions, the formation of stable N-nH $(n \geq 2)$ complexes [26,27] results in the neutralization of all the effects of N incorporation on the optical and electronic properties of the host material [20,28–31]. The N-induced energy-gap redshift, in particular, is fully passivated upon H irradiation, resulting in the complete recovery of the band gap of the N-free material. Coupled to the ultrasharp diffusion profile of H in dilute nitrides (approximately 5 nm/decade at a hydrogenation temperature $T_H = 200\,°\mathrm{C}$; approximately 10–15 nm/decade at $T_H = 300\,°\mathrm{C}$) [32], the possibility to perform spatially selective hydrogenation—for example by depositing H-opaque metallic masks prior to H irradiation [33,34]—can, therefore, be exploited to define nanometer-sized potential wells, i.e., quantum dots, wherein carriers are quantum confined in all spatial directions [35]. These site-controlled QDs have very recently shown evidence of single-photon emission [36] and are inherently well suited for the integration with nanophotonic devices [9–12,37,38].

In addition to its dramatic effects on the electronic properties of dilute nitrides, however, H irradiation also has a deep influence on the lattice parameter a of the host material. As reported in Refs. [26,27,39,40], indeed, each of the several stable N-nH $(n \geq 2)$ complexes that form in hydrogenated dilute nitrides has been associated with a more or less significant expansion of the host lattice. To be more precise, the formation of the N-2H complex responsible for the electronic passivation of nitrogen [26,41], is known to result in a lattice parameter that is roughly equivalent to that of GaAs (N incorporation originally reduces a) [42], whereas the N-nH $(n \geq 3)$ centers that form when one or more H atoms get trapped in the proximity of a strongly bound N-2H complex lead to an even larger lattice expansion [26,39,40]. As a consequence of this expansion, the strain state of a $\mathrm{GaAs}_{1-x}\mathrm{N}_x/\mathrm{GaAs}$ epilayer goes from tensile to compressive following H irradiation. When coupled to the spatially selective-hydrogenation technique introduced in the previous paragraph, this effect can be harnessed to introduce a controlled modulation in the strain profile of the sample. In turn, such modulation can be exploited to tailor the (highly strain-dependent) mixing between heavy-hole (HH) and light-hole (LH) valence-band states, thus allowing for a fine-tuning of the optical properties of the material.

A striking demonstration of this concept is described in the present work, wherein we discuss how the creation of an ordered pattern of H-free dilute-nitride wires, surrounded by fully hydrogenated barriers, results in the introduction of a high degree of linear polarization in the light emitted by a $\mathrm{GaAs}_{1-x}\mathrm{N}_x/\mathrm{GaAs}$ epilayer. Furthermore, by rotating the wire pattern at several angles in the growth plane of the epilayer, we find that the polarization orientation follows that of the wires—albeit in a nontrivial manner—and that the polarization degree is also strongly dependent on the relative orientation of the wires with respect to the high-symmetry axes of the underlying crystal. These experimental findings, well reproduced by a theoretical model based on finite-element calculations of the strain profile in the patterned epilayer, underline the potential of spatially selective hydrogenation as a powerful strain-engineering tool. Moreover, the possibility to freely adjust the angle and the degree of polarization of the light emitted by the micro- (and nano-) structures fabricated with this method will be beneficial to studies [43,44] requiring a precise tuning of the coupling between the active medium and the (typically strongly polarized [38,45]) modes of an optical microcavity (based, e.g., on photonic crystals, PhCs), as well as for applications where polarization sensitivity is still an issue, such as wideband-semiconductor optical amplifiers [46].

II. WIRE FABRICATION AND MODELING

The procedure employed to fabricate the wire patterns described in this work is outlined in Fig. 1. Five different arrays of 500-nm-wide H-opaque Ti wires (wire-to-wire spacing of 5 μm) are deposited on the surface of a $\mathrm{GaAs}_{1-x}\mathrm{N}_x/\mathrm{GaAs}$ epilayer [Fig. 1(a); N concentration $x = 0.8\%$, epilayer thickness of 200 nm]. For each pattern, the metallic wires are oriented at a different angle, 45° (that is, parallel to the [110] direction), 23°, 0°, −22°, and −45° (i.e., parallel to the $[1\bar{1}0]$ axis) with respect to the [100] crystallographic direction (Fig. 1 refers to a wire oriented at 0°). Following mask deposition, the sample is irradiated with low-energy (100 eV) H^+ ions [Fig. 1(b)], resulting in the formation of strained $\mathrm{GaAs}_{1-x}\mathrm{N}_x/\mathrm{GaAs}_{1-x}\mathrm{N}_x{:}\mathrm{H}$ wires [Fig. 1(c)]. H irradiation is performed via a Kaufman source, with the sample kept at a temperature $T_H = 300\,°\mathrm{C}$ to increase H diffusion. Figures 1(b) and 1(c) also display the spatial distribution of the effective N concentration x_{eff} (i.e., of the concentration of unpassivated N atoms) at two different hydrogenation times ($t_H = 5000$ s and $t_H = 10\,000$ s, the latter selected to match the total experimental hydrogenation time). These concentration maps are obtained by performing finite-element calculations based on the model of H diffusion introduced in Ref. [32]. In this model, the N-nH complexes $(n \leq 3)$ formed following H

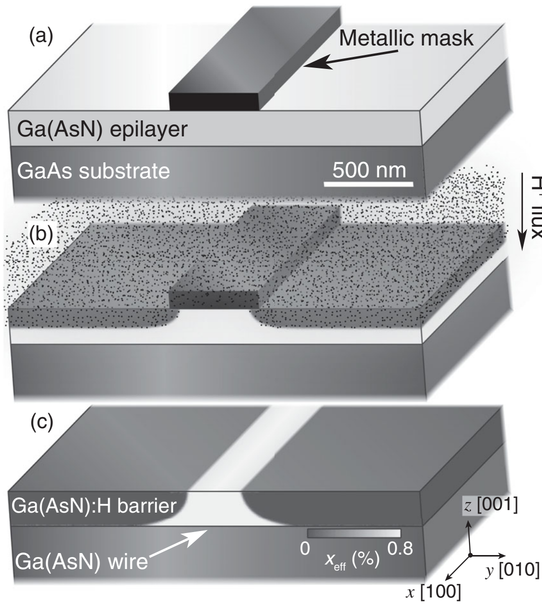

FIG. 1. (a)–(c) Sketch of the process of spatially selective hydrogenation. Following the deposition of a H-opaque Ti mask (a), the sample is hydrogenated (b) at a temperature $T_H = 300\,°\mathrm{C}$. Then, the Ti mask is removed (c), leaving a $\mathrm{GaAs}_{1-x}\mathrm{N}_x$ wire embedded in a (GaAs-like) $\mathrm{GaAs}_{1-x}\mathrm{N}_x{:}\mathrm{H}$ barrier (the wire is oriented along the [100] axis in this sketch). The effective N concentration (x_{eff}, corresponding to the concentration of unpassivated N atoms) distributions displayed as a gray scale in (b) and (c) are the result of finite-element calculations based on the model of H diffusion introduced in Ref. [32] and correspond to hydrogenation times of 5000 and of 10 000 s, respectively ($T_H = 300\,°\mathrm{C}$). The coordinate system established in (c) will be employed throughout the remainder of this work.

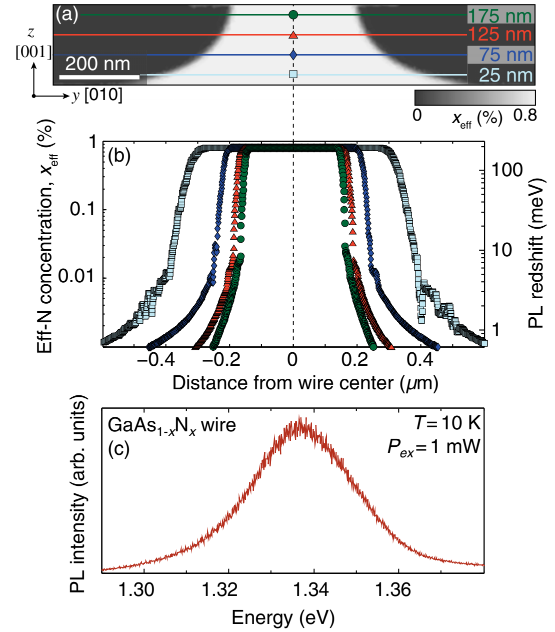

FIG. 2. (a) Expanded view of the spatial distribution of the effective N concentration (x_{eff}) in the plane perpendicular to a $\mathrm{GaAs}_{1-x}\mathrm{N}_x/\mathrm{GaAs}_{1-x}\mathrm{N}_x{:}\mathrm{H}$ wire [i.e., in the yz plane; see, also, Fig. 1(c)]. (b) x_{eff} profiles along the horizontal lines displayed in (a), placed at four different points along the wire height (from bottom to top: light blue squares at 25 nm from the wire bottom; dark blue diamonds at 75 nm; red triangles at 125 nm; green circles at 175 nm). The N-induced photoluminescence (PL) redshift corresponding to each value of x_{eff} is reported on the right-hand axis. (c) Nonpolarized micro-PL spectrum (temperature $T = 10$ K; excitation power density approximately $100\ \mathrm{kW/cm^2}$) of a single $\mathrm{GaAs}_{1-x}\mathrm{N}_x/\mathrm{GaAs}_{1-x}\mathrm{N}_x{:}\mathrm{H}$ wire oriented at 45° (i.e., parallel to the [110] direction).

irradiation of $\mathrm{GaAs}_{1-x}\mathrm{N}_x$ are treated as distinct species, whose concentrations—together with the concentrations of “free” (i.e., not bound to one another) N and H—can be found separately by solving a system of diffusion-reaction equations [32,47]. Both in practice and in the calculations, the total hydrogenation time is set to ensure that, in the regions away from the H-opaque metallic masks, the H-diffusion profile will stop precisely at the interface between the $\mathrm{GaAs}_{1-x}\mathrm{N}_x$ epilayer and the underlying GaAs substrate. The mask width $w = 500$ nm is selected to strike a balance between two contrasting trends. On the one hand, the polarization degree of the light emitted by these structures has been reported to increase in laterally thinner wires [48]. On the other hand, for smaller mask widths and for the optimized hydrogenation conditions used in the present work, H diffuses all the way underneath the mask, resulting in a thinning of the wire in the vertical direction. In turn, this yields a significant degradation of the polarization degree of the wire emission, due to (i) a marked loss of verticality of the wire’s sidewalls and (ii) the appearance of quantum-confinement effects in the structures [49]. For $w = 500$ nm, however, the wires resulting from the spatially selective-hydrogenation procedure summarized in Fig. 1 have a characteristic bell-bottomed shape, with a very sharp interface between H-free and fully hydrogenated regions. As displayed in Figs. 2(a) and 2(b), indeed, in the upper region of the wire—down to approximately 100 nm below the sample surface, where the wire-barrier interface is still nearly vertical and the wire has not yet begun to “flare out” towards the bottom of the epilayer—the effective N concentration decreases by 2 orders of magnitude within less than 40 nm. Such a sharp dropoff in x_{eff} ensures that each wire can be seen as an individual, well-defined entity characterized, among other things, by a photoluminescence (PL) peak [see Fig. 2(c)] that lies approximately 200 meV below the emission energy of the surrounding GaAs-like barriers (1.515 eV at $T = 10$ K). The N-induced PL redshift associated with a given value of x_{eff}—$\Delta E_g(x_{\mathrm{eff}}) = -(12.1\ \mathrm{eV})(x_{\mathrm{eff}})^{0.86}$, obtained by fitting a power law to the values of the energy of the PL peak measured in a series of $\mathrm{GaAs}_{1-x}\mathrm{N}_x/\mathrm{GaAs}$ epilayers with $x \leq 0.8\%$—is displayed on the right-hand axis of Fig. 2(b).

Because of the effects of H irradiation on the lattice parameter of dilute nitrides, the presence of very large gradients in the spatial distribution of the effective N

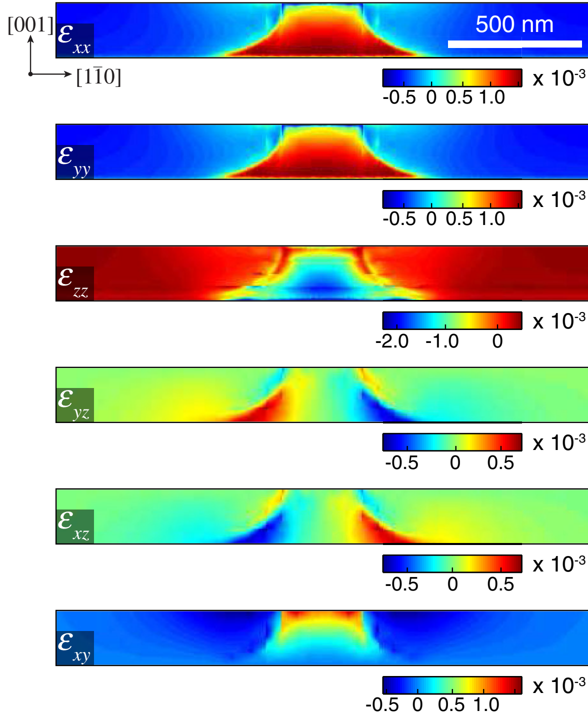

FIG. 3. Spatial distribution (in the plane perpendicular to the wire) of the six components of the elastic strain tensor ε in proximity of a $GaAs_{1-x}N_x/GaAs_{1-x}N_x$:H wire oriented along the [110] crystallographic axis.

concentration also results in the creation of a significant and fully controllable strain anisotropy in the selectively hydrogenated $GaAs_{1-x}N_x/GaAs$ epilayer. Such anisotropy is self-evident in Fig. 3, which displays the spatial distribution of the six components of the elastic strain tensor $\varepsilon\,[=(\varepsilon_{xx}, \varepsilon_{yy}, \varepsilon_{zz}, \varepsilon_{yz}, \varepsilon_{xz}, \varepsilon_{xy})]$ in the plane perpendicular to a $GaAs_{1-x}N_x/GaAs_{1-x}N_x$:H wire oriented along the [110] crystallographic axis (in the reference system employed here and throughout the remainder of this work, the x, y, and z axes correspond to the [100], [010], and [001] directions; see, also, Fig. 1). By virtue of the availability of the individual concentration distributions for each of the N-nH ($n = 2, 3$) complexes responsible for N passivation—the computation of which was a key step in the construction of the effective N concentration profile presented in Figs. 1(c) and 2 (see above)—we are able to evaluate the contribution of each complex species to the lattice expansion on a point-by-point basis. In turn, this provides us with an excellent starting point for the computation of accurate strain maps of the $GaAs_{1-x}N_x/GaAs_{1-x}N_x$:H wires, again via the finite-element method (FEM). It is worth noting that such computation has to be performed only for the wire oriented at 0° with respect to the [100] direction. The derivation of the elastic strain tensor for the other wire orientations is rather straightforward, and it is obtained by applying the proper rotation operator to the computed ε (see Ref. [4] for more details).

III. RESULTS AND DISCUSSION

As briefly discussed in the introductory paragraphs, the presence of strain anisotropies as pronounced as those displayed in Fig. 3 is expected to yield large nontrivial effects on the polarization properties of the light emitted by the material. In order to investigate these effects, we perform low-temperature ($T = 10$ and 80 K) polarization-resolved micro-PL measurements on a set of single $GaAs_{1-x}N_x/GaAs_{1-x}N_x$:H wires of varying orientation. The sample, mounted in a He-flow cryostat, is excited with a frequency-doubled Nd:YVO_4 laser (excitation wavelength $\lambda_{ex} = 532$ nm, laser power $P_{ex} = 1$ mW) focused on the sample through a 50× microscope objective (numerical aperture of 0.5), thus resulting in a spot size of approximately 1 μm. The PL signal is then collected through the same objective and spectrally analyzed with a single-grating 75-cm-long monochromator coupled to a N_2-cooled Si CCD detector. Access to the polarization properties of the micro-PL signal coming from the wires is attained by placing a half-wave plate—followed by a linear polarizer—in the detection path [50]. It is important to note that in this configuration, the actual polarization of the detected photons is fixed by the orientation of the linear polarizer, so that the polarization response of the detection setup can be disregarded. By progressively rotating the slow axis of the plate with respect to the polarizer, we can collect the full dependence of the PL intensity on the angle that the polarization vector forms with the [100] crystallographic axis. The results of these measurements for single $GaAs_{1-x}N_x/GaAs_{1-x}N_x$:H wires of five different orientations (45°, 23°, 0°, −22°, and −45°) are summarized in Fig. 4. The wire emission is characterized by a high degree of linear polarization; moreover, the polarization direction very clearly rotates with the wire orientation. For wires oriented along axes of high crystalline symmetry, i.e., along the [110], [100], and [1$\bar{1}$0] directions (that is, at 45°, 0°, and −45°) the polarization angle α is precisely at 90° with respect to the wire [48]; for the wires oriented at 23° and −22°, however, there are sizeable deviations from a perfect orthogonality. In addition, the polarization degree ρ of the wire emission displays a strong dependence on both the wire orientation—with maxima at ±45° and a minimum at 0°—and the sample temperature, with a significant decrease in the measured value of ρ when T is raised from 10 to 80 K.

In order to understand the microscopic origin of the observed dependence of the polarization properties on the wire orientation (as well as on temperature), it is extremely interesting to compare the values of ρ and α determined experimentally with those theoretically expected for the strained wire structures. The effects of strain on the Γ ($\vec{k} = 0$) point of the conduction (CB) and (light- and heavy-hole) valence bands (VB) of a semiconductor are, indeed, well reproduced by the Bir-Pikus Hamiltonian [4,51]:

$$H_c(\vec{k} = 0) = E_g(x_{\rm eff}) - |a_c|(\varepsilon_{xx} + \varepsilon_{yy} + \varepsilon_{zz}) \quad (1)$$

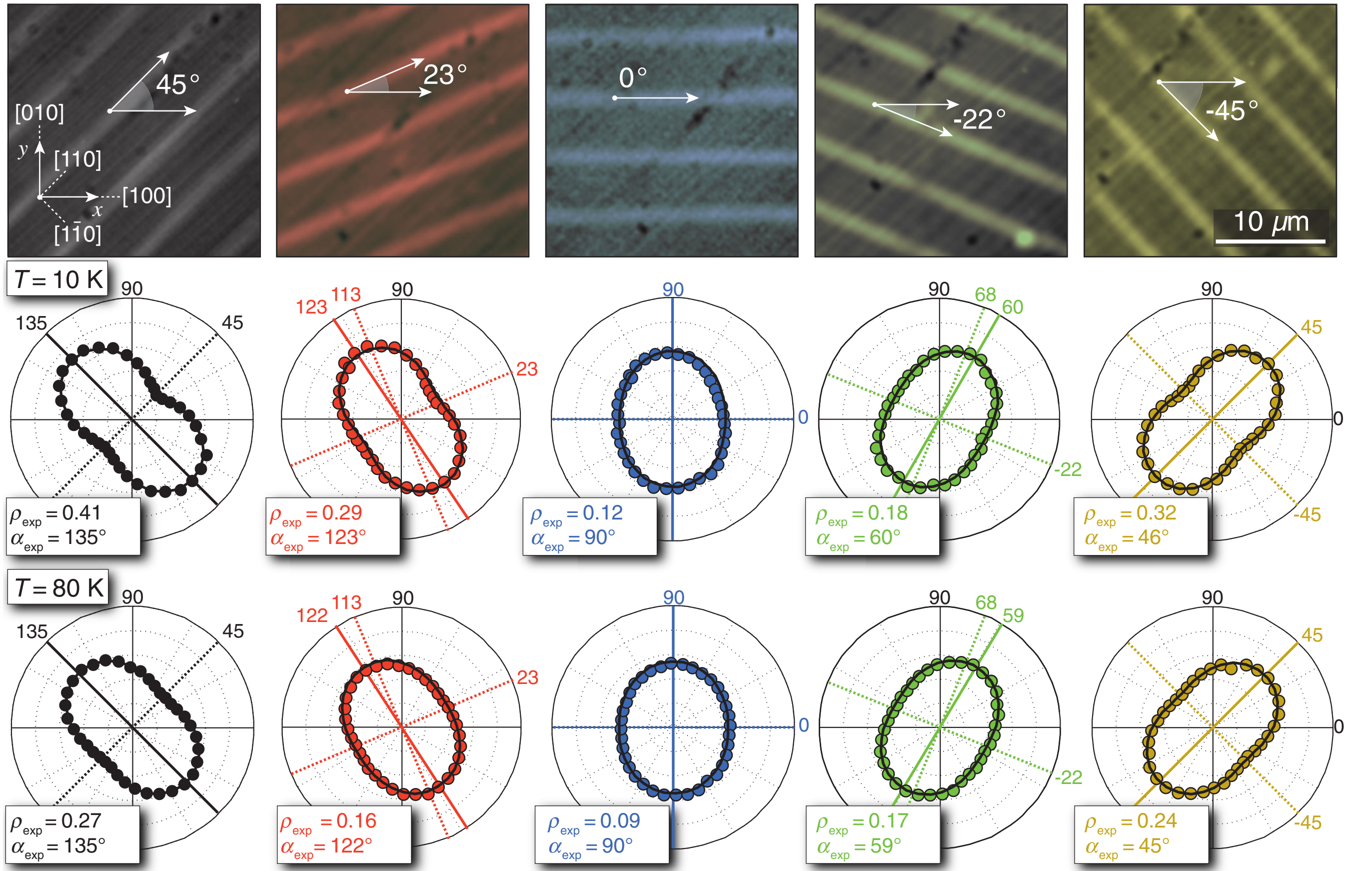

FIG. 4. Top: False-color micro-PL images (acquired at a temperature $T = 80$ K; the contribution of the substrate and of the hydrogenated barriers is filtered out with an 850-nm longpass filter) of the light emitted by arrays of $GaAs_{1-x}N_x/GaAs_{1-x}N_x:H$ wires oriented at 45° (black), 23° (red), 0° (blue), −22° (green), and −45° (yellow) with respect to the [100] axis of the underlying crystal. Center: Polar plots of the micro-PL intensity ($T = 10$ K) of single $GaAs_{1-x}N_x/GaAs_{1-x}N_x:H$ wires of different orientations, acquired as a function of the angle θ between the polarization vector and the [100] crystallographic axis. The experimental data points are plotted as circles (having the same filling color as their corresponding micro-PL image; see above), while fitting curves based on Malus's law are displayed as solid lines. The values of the degree ($\rho_{\rm exp}$) and angle ($\alpha_{\rm exp}$) of linear polarization obtained from the fits are also reported for each wire orientation. Bottom: Same as above but for $T = 80$ K.

and

$$H_v(\vec{k}=0) = -\begin{pmatrix} P+Q & -S & R & 0 \\ -S^+ & P-Q & 0 & R \\ R^+ & 0 & P-Q & S \\ 0 & R^+ & S^+ & P+Q \end{pmatrix}, \tag{2}$$

where H_c and H_v refer to the conduction and valence band, respectively, and

$$\begin{aligned} P &= -|a_v|(\varepsilon_{xx}+\varepsilon_{yy}+\varepsilon_{zz}), \\ Q &= \frac{|b|}{2}(\varepsilon_{xx}+\varepsilon_{yy}-2\varepsilon_{zz}), \\ R &= -\frac{\sqrt{3}}{2}|b|(\varepsilon_{xx}-\varepsilon_{yy})+i|d|\varepsilon_{xy}, \\ S &= |d|(\varepsilon_{xz}-i\varepsilon_{yz}). \end{aligned} \tag{3}$$

In Eqs. (1)–(3), $E_g(x_{\rm eff}) = E_g^{\rm GaAs} + \Delta E_g(x_{\rm eff})$ [see above for the definition of $\Delta E_g(x_{\rm eff})$; $E_g^{\rm GaAs}$ is the energy gap of GaAs] is the energy gap of a $GaAs_{1-x}N_x/GaAs$ epilayer having effective N concentration $x_{\rm eff}$, while $a_c = -7.17$ eV, $a_v = -1.16$ eV, $b = -2.0$ eV, and $d = -4.8$ eV are the deformation potentials of GaAs [52]. These equations establish a direct link between the geometry of our strained system—expressed via the different components of the strain tensor ε (see Fig. 3)—and its CB [Eq. (1)] and VB [Eqs. (2) and (3)] states. Within this context, it is interesting to note how the nondiagonal terms of H_v, which ultimately determine the degree of HH-LH mixing characterizing the eigenstates of the system, depend directly on the nondiagonal components of the strain tensor as well as on the difference between ε_{xx} and ε_{yy} (it should be noted that $\varepsilon_{xx} - \varepsilon_{yy} = 0$ for biaxial and isotropic strain).

By inserting the computed values of ε and $x_{\rm eff}$ (see Fig. 2) in Eqs. (1)–(3), we can obtain the CB and VB eigenenergies and eigenstates in every point of our

$GaAs_{1-x}N_x/GaAs_{1-x}N_x$:H wires. According to these calculations, the presence of a degeneracy in the 4×4 H_v matrix results in a two-way splitting of the valence band maximum of the strained material. This splitting ultimately gives rise to two peaks in the emission spectrum of the wire, having energy

$$E_{1,2} = E_g(x_{\rm eff}) - E_b^X - |a_c|(\varepsilon_{xx} + \varepsilon_{yy} + \varepsilon_{zz}) + P \mp \sqrt{Q^2 + R^2 + S^2}. \quad (4)$$

Excitonic effects (which are not included in the Bir-Pikus Hamiltonian) are effectively accounted for by subtracting E_b^X, the exciton binding energy, from $E_{1,2}$ [53]. In order to evaluate the probability $P_{1,2}(\theta)$ that a photon with energy $E_{1,2}$—and polarization vector $\hat{e}$ oriented at an angle θ with respect to the [100] crystallographic direction—is emitted by the wire, on the other hand, one has to compute the square of the matrix elements of the light-matter interaction Hamiltonian H' between the relevant conduction- and valence-band eigenstates. The simple consideration of the fact that, in the dipole approximation, H' is proportional to $\hat{e}\cdot\vec{p}$ (where $\vec{p}$ is the momentum operator) allows for justifying, in very intuitive terms, the presence of a strong dependence of $P_{1,2}(\theta)$ on the polarization orientation θ. In order to estimate the way in which such a dependence does, indeed, influence the polarization properties of the wire emission, $P_{1,2}(\theta)$ must, in turn, be weighted with the corresponding reduced density of states—proportional to $\mu_{1,2}^{3/2}$, where $\mu_{1,2}$ is the exciton reduced mass—and with the relative thermal occupation probability of the valence-band states involved in the transitions having energy E_1 and E_2 [48]:

$$I_1(\theta) \propto \mu_1^{3/2} P_1(\theta), \qquad I_2(\theta) \propto \mu_2^{3/2} P_2(\theta) e^{-\frac{\Delta E_{1,2}}{k_B T_c}}. \quad (5)$$

Here, $I_{1,2}(\theta)$ is the intensity of the light emitted with energy $E_{1,2}$, whereas k_B is the Boltzmann constant, and $\Delta E_{1,2}$ is the difference between E_2 and E_1. In all the calculations presented here, we use the value $\frac{\mu_2}{\mu_1} = 1.2$, as proposed in Ref. [48]. It is important to note that, rather than using the nominal lattice temperature T, in Eq. (5) the carrier temperature T_c is employed to estimate the thermal population of the valence-band states. As we will discuss in greater detail in the final part of this article, the introduction of a distinction between T and T_c (with $T_c > T$) is a necessity in experimental situations, such as this one, for which the use of high power densities (approximately 100 kW/cm^2 in our case, largely as a consequence of the approximately 1-μm spot size typical of the micro-PL setup we employ) results in a significant overpopulation of the higher-energy levels of the investigated system with respect to what would be expected if photogenerated carriers were at thermal equilibrium with the lattice.

As mentioned above, the coupling of Eqs. (4) and (5) with the point-by-point spatial maps of ϵ and $x_{\rm eff}$ previously obtained via FEM calculations (see Figs. 2 and 3) allows us to compute the values of E_1^j, E_2^j, $I_1^j(\theta)$, and $I_2^j(\theta)$ at the jth point ($j = 1, \ldots, N$) of our strained structures. In turn, these quantities can be combined as follows:

$$\mathbf{I}_1(E,\theta) = \sum_{j=1,\ldots,N}^{|E-E_1^j|\leq 1\ \text{meV}} I_1^j(\theta),$$

$$\mathbf{I}_2(E,\theta) = \sum_{j=1,\ldots,N}^{|E-E_2^j|\leq 1\ \text{meV}} I_2^j(\theta) \quad (6)$$

to estimate the expected energy (and angular) dependence of the intensity of the lower- $[\mathbf{I}_1(E,\theta)]$ and higher-energy $[\mathbf{I}_2(E,\theta)]$ transitions making up the emission of a $GaAs_{1-x}N_x/GaAs_{1-x}N_x$:H wire. The total wire intensity $\mathbf{I}_{\rm tot}$ can finally be obtained as

$$\mathbf{I}_{\rm tot}(E,\theta) = \mathbf{I}_1(E,\theta) + \mathbf{I}_2(E,\theta). \quad (7)$$

As summarized in Fig. 5, which refers to the intensity of the light emitted by a wire oriented at 23° with respect to

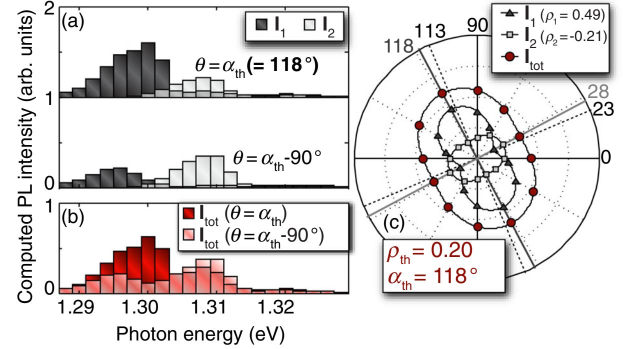

FIG. 5. (a) Bar plots (bar width, 2 meV) of the computed energy dependence [at $T_c = 80$ K; see Eqs. (5) and (6)] of the intensity of the low- ($\mathbf{I}_1$, dark gray) and high-energy ($\mathbf{I}_2$, light gray) transitions that make up the emission of a $GaAs_{1-x}N_x/GaAs_{1-x}N_x$:H wire oriented at 23° with respect to the [100] crystallographic axis. For the plots shown in the upper (lower) part of the panel, the angle θ formed by the polarization vector and the [100] direction is set at $\alpha_{\rm th} = 118°$ ($\alpha_{\rm th} - 90° = 28°$); i.e., the angle for which the total computed intensity $\mathbf{I}_{\rm tot} = \mathbf{I}_1 + \mathbf{I}_2$ is maximal (minimal). The plot relative to $\theta = \alpha_{\rm th}$ is vertically shifted for clarity. (b) Bar plots (bar width, 2 meV) of the computed energy dependence of $\mathbf{I}_{\rm tot}$. The computed spectra corresponding to $\theta = \alpha_{\rm th}$ (118°, dark red) and $\theta = \alpha_{\rm th} - 90°$ (28°, light red) are shown. (c) Polar plots of the computed dependence of $\mathbf{I}_1$ (dark gray triangles), $\mathbf{I}_2$ (light gray squares), and $\mathbf{I}_{\rm tot}$ (dark red circles) on the angle θ between the polarization vector and the [100] crystallographic axis. In order to construct the curves reported in this panel, the computed intensities are integrated over the whole 40-meV energy interval displayed in panels (a) and (b).

the [100] axis (computed with $T_c = 80$ K), $\mathbf{I}_1$ and $\mathbf{I}_2$ are characterized by significant degrees of linear polarization—labeled as ρ_1 and ρ_2, respectively—and by mutually orthogonal polarization directions [see Fig. 5(c)]. As a consequence of the latter property, which holds true for all wire orientations, the computed polarization angle of the total wire emission α_{th} does not depend on the temperature. The total polarization degree ρ_{th}, on the other hand, decreases progressively as T_c increases, and the weight of $\mathbf{I}_2$ becomes comparable to that of $\mathbf{I}_1$. As Eq. (5) clearly suggests, the most relevant parameter for the determination of the temperature sensitivity of the wires' polarization degree is represented by $\Delta E_{1,2}$, the splitting between the higher- and lower-energy wire transitions. For the wires investigated here, the average value of $\Delta E_{1,2}$ is approximately 10.5 meV, with a very weak dependence on the wire orientation. A relatively straightforward manner for increasing $\Delta E_{1,2}$, thereby making the polarization properties of $\mathrm{GaAs}_{1-x}\mathrm{N}_x/\mathrm{GaAs}_{1-x}\mathrm{N}_x\colon\mathrm{H}$ wires more robust to temperature variations, is represented by the possibility of employing $\mathrm{GaAs}_{1-x}\mathrm{N}_x$ epilayers with higher N concentration (samples with good optical quality and $x \leq 4\%$ are reported in the literature [54]). However, it is worth mentioning here that the absolute value of ρ_1, ranging between 0.51 (for wires oriented along the $\langle 110\rangle$ directions) and 0.45 (for wires parallel to the $\langle 100\rangle$ axis), is always significantly larger than that of ρ_2, which varies between -0.22 and -0.19 for the wire orientations considered here. This justifies the persistence of a significant polarization degree with increasing temperature, which is apparent from the $T = 80$ K data displayed in Figs. 4 and 6 and is also consistent with the $\rho = 0.2$ value reported in Ref. [48] for $\mathrm{GaAs}_{1-x}\mathrm{N}_x/\mathrm{GaAs}_{1-x}\mathrm{N}_x\colon\mathrm{H}$ wires ($x = 0.9\%$, $w = 500$ nm) measured at room temperature.

Also of note is the fact that for the example displayed in Fig. 5—which is representative of a generic wire orientation, not parallel to any of the high-symmetry $\langle 100\rangle$ or $\langle 110\rangle$ directions—the polarization direction $\alpha_{\mathrm{th}} = 118°$ is not precisely perpendicular to the wire orientation ($23° + 90° = 113°$), in good qualitative agreement with the experimental results summarized in Fig. 4 (for the wire oriented at 23°, we find $\alpha = 123°$ and 122° for measurements performed at 10 and 80 K, respectively). Furthermore, the value of the polarization degree reported in Fig. 5—$\rho_{\mathrm{th}} = 0.20$ for the wire oriented at 23° and for $T_c = 80$ K—also agrees well with the experimentally determined value ($\rho = 0.16$ at $T = 80$ K). Incidentally, this also seems to suggest that, for measurements performed at $T = 80$ K, photogenerated carriers may be close to thermal equilibrium with the lattice, i.e., $T \sim T_c$.

In order to compare the results of our calculations with a statistically more significant estimate of the polarization properties of our wire arrays, we randomly select a set of ten $\mathrm{GaAs}_{1-x}\mathrm{N}_x/\mathrm{GaAs}_{1-x}\mathrm{N}_x\colon\mathrm{H}$ wires for each orientation. For every one of these ten wires, we acquire micro-PL

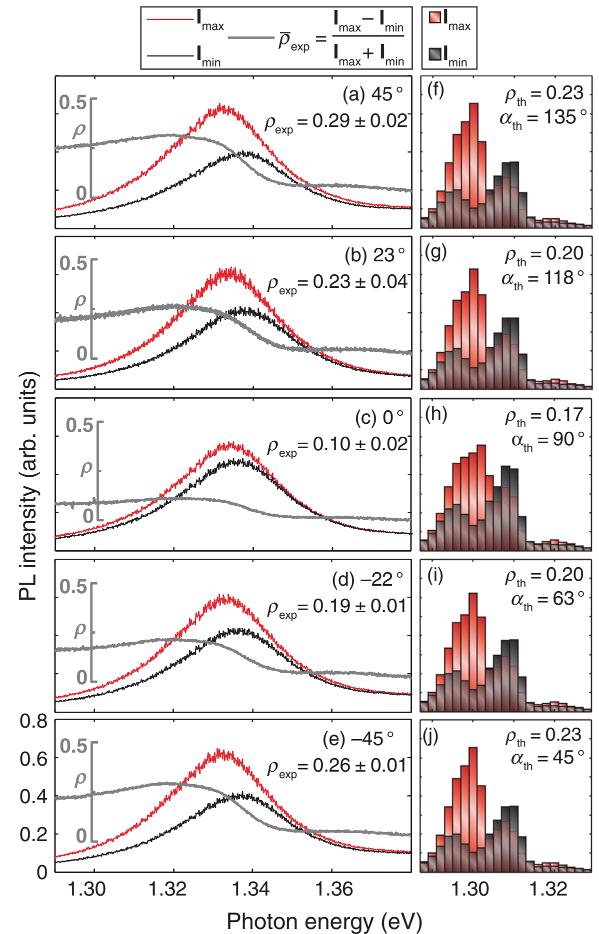

FIG. 6. (a)–(e) Average (see main text) PL spectra (temperature $T = 80$ K) of the $\mathrm{GaAs}_{1-x}\mathrm{N}_x/\mathrm{GaAs}_{1-x}\mathrm{N}_x\colon\mathrm{H}$ wires oriented at 45° (a), 23° (b), 0° (c), −22° (d), and −45° (e) with respect to the [100] direction. For each orientation, the spectra relative to the polarization angles corresponding to the maximal ($\mathbf{I}_{\max}$, red line) and minimal ($\mathbf{I}_{\min}$, black line) PL intensity are shown, together with the average energy-dependent degree of linear polarization ($\bar{\rho}_{\mathrm{exp}}$, gray line). (f)–(j) Bar plots (bar width, 2 meV) of the energy dependence of the wire emission calculated through Eq. (7) ($T_c = 80$ K; see main text). As in the case of the experimental spectra, the maximum- (red bars) and minimum-intensity (black bars) spectra are shown for each wire orientation, together with the calculated values of the degree (ρ_{th}) and angle (α_{th}) of linear polarization. The approximate 30-meV blueshift that can be observed between the experimental spectra and the computed ones is likely another effect of the saturation of the energy levels of the wire due to the high power density (approximately $100\ \mathrm{kW/cm^2}$) employed in our micro-PL measurements (see main text). In this respect, it should be noted that the estimated dependence of the energy gap on the effective N concentration that is used in the computations $E_g(x_{\mathrm{eff}})$ is, indeed, obtained from conventional macro-PL measurements, performed with a large excitation laser spot (approximately 200 μm) and with a power density (approximately $30\ \mathrm{W/cm^2}$) more than 3 orders of magnitude lower than the one used for the measurements summarized in (a)–(e).

spectra at the polarization angles corresponding to the maximal ($\mathbf{I}_{max}$) and minimal ($\mathbf{I}_{min}$) PL intensity. Afterwards, we construct an "average" PL spectrum for each wire orientation and polarization angle, by summing over the corresponding ten single-wire spectra. First of all, it is interesting to note that these average curves, displayed in Figs. 6(a)–6(e) for $T = 80$ K, are not appreciably broadened with respect to their corresponding single-wire spectra [see, for example, Fig. 2(c)]. This observation points to a very good wire-to-wire homogeneity, highlighting the excellent quality of our fabrication process. Also, through these spectra it is possible to estimate an average polarization degree

$$\bar{\rho}_{\rm exp} = \frac{\mathbf{I}_{max} - \mathbf{I}_{min}}{\mathbf{I}_{max} + \mathbf{I}_{min}} \quad (8)$$

for each wire orientation [the numerical value of the polarization degree, also provided in Figs. 6(a)–6(e), is obtained by integrating $\bar{\rho}_{\rm exp}$ over a 40-meV interval centered on the energy corresponding to the maximal value of ρ]. The values of $\bar{\rho}_{\rm exp}$ obtained with this method are in good agreement with those reported in Fig. 4 and confirm the presence of a clear minimum of the polarization degree for wires oriented at 0°, together with two maxima at ±45°. Finally, the average PL spectra presented in Figs. 6(a)–6(e) can be directly compared with the computed energy dependence of the total wire intensity ($\mathbf{I}_{tot}$), obtained via Eq. (7) and displayed in Figs. 6(f)–6(j) for the five orientations investigated here. As in the case of the experimental results, for each wire pattern we plot the "computed spectra" for the polarization angles corresponding to the maximal and minimal emission intensity. For all wire orientations the computed polarization angle (α_{th}) and polarization degree (ρ_{th}), obtained from the simulated spectra by averaging over the 40-meV energy interval (1.288–1.328 eV) displayed in Figs. 6(f)–6(j), both reproduce the trends detected in the experimental data in a rather convincing manner.

Figure 7 summarizes the dependence of ρ and α on the wire orientation for the two temperatures ($T = 10$ and 80 K) at which the measurements are performed, thus providing a more complete picture of the generally good agreement between the results of our calculations and the experimental data. At the same time, the data sets displayed in the figure also uncover a few discrepancies between theory and experiments, which are worth discussing here. First of all, in agreement with the potential scenario we outlined in the discussion of Eq. (5), at 10 K the rather high power densities at which our measurements are performed (approximately 100 kW/cm^2, mostly due to the approximately 1-μm spot size inherent to our micro-PL configuration) result in a significant overpopulation of the higher-energy wire levels, reflected by the need to set T_c to a value considerably higher than T ($T_c = 50$ K) in order to

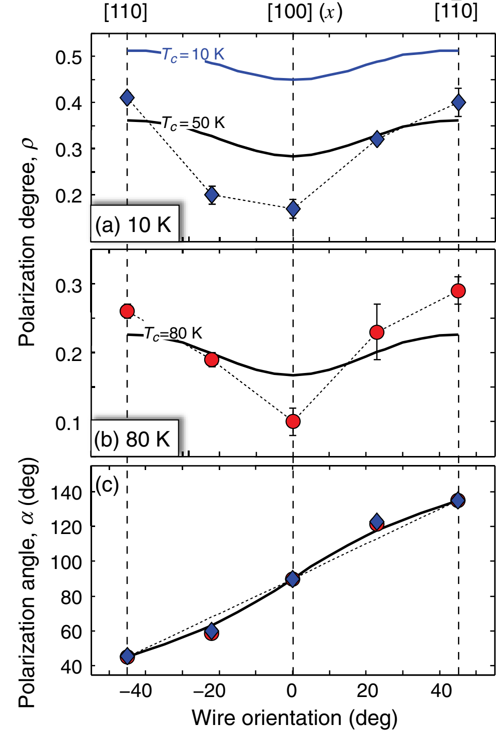

FIG. 7. (a) Dependence of the degree of linear polarization ρ on the wire orientation. The experimental data (acquired at a temperature $T = 10$ K) are shown as blue diamonds (the thin-dotted line is a guide to the eye), while the values of ρ calculated at a carrier temperature of $T_c = 10$ K ($T_c = 50$ K) are plotted as a solid blue (black) line. (b) Same as (a) for $T = 80$ K. The experimental data are displayed as red circles, while the calculated values of ρ ($T_c = 80$ K) are shown as a solid black line. (c) Dependence of the angle of linear polarization α on the wire orientation. The experimental data acquired at $T = 10$ K ($T = 80$ K) are shown as blue diamonds (red circles), whereas the calculated polarization angle is plotted as a solid black line. The dotted black line represents the angle perpendicular to the wire orientation and is provided as a reference.

maximize the agreement of our calculations with the experimental results [see Fig. 7(a)]. Even moderately higher temperatures, on the other hand, are seemingly sufficient to reestablish thermal equilibrium between the photogenerated carriers and the lattice, so that, at $T = 80$ K, the best agreement between calculations and experiments is achieved by setting $T = T_c$ [as shown in Fig. 7(b)]. It should be noted that the fact that the agreement between experiments and theory arguably improves with increasing temperature might also be related to the presence of localized states, which, albeit not taken into account in our calculations, have been widely reported to play a large role in the emission of $GaAs_{1-x}N_x$-based samples [55], particularly at low T.

In addition, both the minimum of ρ observed for the wires oriented at 0° [see Figs. 7(a) and 7(b)] and, to a lesser extent, the deviations of α from the normal to the wire for structures not oriented at ±45° or at 0° [see Fig. 7(c)]

are more pronounced in the experimental data than in the computed curves. This stronger-than-expected (with respect to our theoretical predictions) dependence of the measured polarization properties on the wire orientation might point to an exceedingly simplistic modeling of the effects of spatially selective hydrogenation on the strain profile of the material. In particular, our model makes the assumption that, at the microscopic level, H incorporation leads to an isotropic expansion of the crystal lattice [39,40]. However, the Ga-N bonds that get broken due to the formation of the N-nH complexes responsible for N passivation [26,56] are oriented along very specific directions, i.e., the $\langle 111 \rangle$ crystallographic axes. As a consequence, it is not unreasonable to think—even though additional experiments and/or theoretical investigations will be required in order to substantiate this hypothesis—that the H-induced expansion might retain a certain degree of spatial anisotropy, which could ultimately influence the observed dependence of the polarization properties of our $GaAs_{1-x}N_x/GaAs_{1-x}N_x:H$ wires on their orientation.

IV. CONCLUSIONS

To summarize, the surface of a $GaAs_{1-x}N_x/GaAs$ epilayer is patterned with ordered arrays of H-opaque metallic wires, oriented at different angles with respect to the [100] crystallographic direction. The highly anisotropic strain field created following H irradiation, due to the H-induced lattice expansion of the barriers surrounding the unpassivated $GaAs_{1-x}N_x$ regions, is found to induce a correspondingly large polarization anisotropy in the light emitted by the fabricated $GaAs_{1-x}N_x/GaAs_{1-x}N_x:H$ wires. This anisotropy is investigated through extensive polarization-resolved micro-PL measurements, which unveil several peculiarities in the behavior of the wires' polarization properties as a function of temperature and wire orientation. In particular, we discover that the degree of linear polarization of the wire emission goes through a pronounced minimum for wires oriented along the [100] axis, with maxima for wires parallel to the [110] and $[1\bar{1}0]$ directions. Moreover, the polarization angle—precisely perpendicular to the wire when the latter is oriented along high-symmetry crystal directions (i.e., the $\langle 110 \rangle$ and $\langle 100 \rangle$ axes)—is significantly off normal in all other cases. Both of these trends are well reproduced by a theoretical model based on the finite-element analysis of (i) the processes of wire formation via H diffusion (see Figs. 1 and 2) and (ii) the effects of the formation of N-nH complexes on the spatial distribution of strain in our patterned epilayer (see Fig. 3). The results presented here are a striking demonstration of our ability to adjust the polarization properties of dilute-nitride micro- and nanostructures via H-assisted strain engineering. This possibility might prove very useful when trying to optimize the performance of photonic devices based on the (polarization-dependent [38]) coupling strength between a PhC microcavity and a dilute-nitride-based light emitter. Furthermore, as discussed in the introductory paragraphs, x-rays propagating through a deformed crystal potentially undergo very large ($>100\ \mu$m) beam translations (Berry-phase effect; see Refs. [15,16,57]). By allowing for the careful tailoring of the strain fields present in the material, spatially selective hydrogenation has the potential to become a very valuable tool for the realization of advanced x-ray optics applications based on this effect [58].

ACKNOWLEDGMENTS

The authors thank Giorgio Pettinari and Armando Rastelli for helpful discussions. M. F. acknowledges funding by the European Union through the Marie Curie program under Grant No. PIEF-GA-2011-301363. M. F., A. P., and M. C. also acknowledge support from the Italian Ministry for Education, University and Research within the Futuro in Ricerca (FIRB) program (project DeLIGHTeD, Protocollo RBFR12RS1W). Finally, M. C. and A. P. acknowledge funding from Sapienza University of Rome, through Fondi Ateneo 2012 and 2013, respectively.

[1] S. Di Fonzo, W. Jark, S. Lagomarsino, C. Giannini, L. De Caro, A. Cedola, and M. Müller, Non-destructive determination of local strain with 100-nanometre spatial resolution, Nature (London) **403**, 638 (2000).

[2] M. Hÿtch, F. Houdellier, F. Hüe, and E. Snoeck, Nanoscale holographic interferometry for strain measurements in electronic devices, Nature (London) **453**, 1086 (2008).

[3] I. Robinson and R. Harder, Coherent x-ray diffraction imaging of strain at the nanoscale, Nat. Mater. **8**, 291 (2009).

[4] Y. Sun, S. E. Thompson, and T. Nishida, *Strain Effect in Semiconductors* (Springer, New York, 2009).

[5] H. S. Yang, R. Malik, S. Narasimha, Y. Li, R. Divakaruni, P. Agnello, S. Allen, A. Antreasyan, J. C. Arnold, and K. Bandy, Dual stress liner for high performance sub-45 nm gate length SOI CMOS manufacturing, IEDM Tech. Digest **04**, 1075 (2004).

[6] S. E. Thompson, Guangyu Sun, Youn Sung Choi, and T. Nishida, Uniaxial-process-induced strained-Si: Extending the CMOS roadmap, IEEE Trans. Electron Devices **53**, 1010 (2006).

[7] I. N. Stranski and L. Krastanow, Zur Theorie der orientierten Ausscheidung von Ionenkristallen aufeinander, Monatshefte Für Chemie/Chemical Monthly **71**, 351 (1937)

[8] J. Stangl, V. Holy, and G. Bauer, Structural properties of self-organized semiconductor nanostructures, Rev. Mod. Phys. **76**, 725 (2004).

[9] T. Yoshie, A. Scherer, J. Hendrickson, G. Khitrova, H. Gibbs, G. Rupper, C. Ell, O. Shchekin, and D. Deppe, Vacuum Rabi splitting with a single quantum dot in a photonic crystal nanocavity, Nature (London) **432**, 200 (2004).

[10] K. Hennessy, A. Badolato, M. Winger, D. Gerace, M. Atatüre, S. Gulde, S. Fält, E. L. Hu, and A. Imamoğlu,

Quantum nature of a strongly coupled single quantum dot-cavity system, Nature (London) **445**, 896 (2007).

[11] A. J. Shields, Semiconductor quantum light sources, Nat. Photonics **1**, 215 (2007).

[12] C. L. Salter, R. M. Stevenson, I. Farrer, C. A. Nicoll, D. A. Ritchie, and A. J. Shields, An entangled-light-emitting diode, Nature (London) **465**, 594 (2010).

[13] D. L. Huffaker, G. Park, Z. Zou, O. B. Shchekin, and D. G. Deppe, 1.3 μm room-temperature GaAs-based quantum-dot laser, Appl. Phys. Lett. **73**, 2564 (1998).

[14] V. M. Ustinov, A. E. Zhukov, A. Y. Egorov, and N. A. Maleev, *Quantum Dot Lasers* (Oxford University Press, Oxford, 2003).

[15] Y. Kohmura, K. Sawada, S. Fukatsu, and T. Ishikawa, Controlling the propagation of x-ray waves inside a heteroepitaxial crystal containing quantum dots using Berry's phase, Phys. Rev. Lett. **110**, 057402 (2013).

[16] K. Sawada, S. Murakami, and N. Nagaosa, Dynamical diffraction theory for wave packet propagation in deformed crystals, Phys. Rev. Lett. **96**, 154802 (2006).

[17] *Dilute Nitride Semiconductors: Physics and Technology*, edited by M. Henini (Elsevier, Oxford, 2005).

[18] M. Weyers and M. Sato, Growth of GaAsN alloys by low-pressure metalorganic chemical vapor-deposition using plasma-cracked NH3, Appl. Phys. Lett. **62**, 1396 (1993).

[19] W. Shan, W. Walukiewicz, J. W. Ager, E. E. Haller, J. F. Geisz, D. J. Friedman, J. M. Olson, and S. R. Kurtz, Band anticrossing in GaInNAs alloys, Phys. Rev. Lett. **82**, 1221 (1999).

[20] F. Masia, G. Pettinari, A. Polimeni, M. Felici, A. Miriametro, M. Capizzi, A. Lindsay, S. B. Healy, E. P. O'Reilly, A. Cristofoli, G. Bais, M. Piccin, S. Rubini, F. Martelli, A. Franciosi, P. J. Klar, K. Volz, and W. Stolz, Interaction between conduction band edge and nitrogen states probed by carrier effective-mass measurements in $GaAs_{1-x}N_x$, Phys. Rev. B **73**, 073201 (2006).

[21] G. Pettinari, A. Polimeni, F. Masia, R. Trotta, M. Felici, M. Capizzi, T. Niebling, W. Stolz, and P. J. Klar, Electron mass in dilute nitrides and its anomalous dependence on hydrostatic pressure, Phys. Rev. Lett. **98**, 146402 (2007).

[22] D. Thomas, J. Hopfield, and C. Frosch, Isoelectronic traps due to nitrogen in gallium phosphide, Phys. Rev. Lett. **15**, 857 (1965).

[23] X. Liu, M. E. Pistol, L. Samuelson, S. Schwetlick, and W. Seifert, Nitrogen pair luminescence in GaAs, Appl. Phys. Lett. **56**, 1451 (1990).

[24] M. Felici, A. Polimeni, A. Miriametro, M. Capizzi, H. P. Xin, and C. W. Tu, Free carrier and/or exciton trapping by nitrogen pairs in dilute $GaP_{1-x}N_x$, Phys. Rev. B **71**, 045209 (2005).

[25] M. Ikezawa, Y. Sakuma, L. Zhang, Y. Sone, T. Mori, T. Hamano, M. Watanabe, K. Sakoda, and Y. Masumoto, Single-photon generation from a nitrogen impurity center in GaAs, Appl. Phys. Lett. **100**, 042106 (2012).

[26] L. Wen, M. Stavola, W. B. Fowler, R. Trotta, A. Polimeni, M. Capizzi, G. Bisognin, M. Berti, S. Rubini, and F. Martelli, Microscopic origin of compressive strain in hydrogen-irradiated dilute $GaAs_{1-y}N_y$ alloys: Role of N-H-n centers with $n > 2$ and their thermal stability, Phys. Rev. B **86**, 085206 (2012).

[27] M. Berti, G. Bisognin, D. De Salvador, E. Napolitani, S. Vangelista, A. Polimeni, M. Capizzi, F. Boscherini, G. Ciatto, S. Rubini, F. Martelli, and A. Franciosi, Formation and dissolution of D-N complexes in dilute nitrides, Phys. Rev. B **76**, 205323 (2007).

[28] A. Polimeni, G. Baldassarri, M. Bissiri, M. Capizzi, M. Fischer, M. Reinhardt, and A. Forchel, Effect of hydrogen on the electronic properties of $In_xGa_{1-x}As_{1-y}N_y/GaAs$ quantum wells, Phys. Rev. B **63**, 201304 (2001).

[29] A. Polimeni, M. Bissiri, M. Felici, M. Capizzi, I. Buyanova, W. Chen, H. Xin, and C. Tu, Nitrogen passivation induced by atomic hydrogen: The $GaP_{1-y}N_y$ case, Phys. Rev. B **67**, 201303 (2003).

[30] G. Pettinari, F. Masia, A. Polimeni, M. Felici, A. Frova, M. Capizzi, A. Lindsay, E. P. O'Reilly, P. J. Klar, W. Stolz, G. Bais, M. Piccin, S. Rubini, F. Martelli, and A. Franciosi, Influence of nitrogen-cluster states on the gyromagnetic factor of electrons in $GaAs_{1-x}N_x$, Phys. Rev. B **74**, 245202 (2006).

[31] M. Geddo, T. Ciabattoni, G. Guizzetti, M. Galli, M. Patrini, A. Polimeni, R. Trotta, M. Capizzi, G. Bais, M. Piccin, S. Rubini, F. Martelli, and A. Franciosi, Photoreflectance and reflectance investigation of deuterium-irradiated GaAsN, Appl. Phys. Lett. **90**, 091907 (2007).

[32] R. Trotta, D. Giubertoni, A. Polimeni, M. Bersani, M. Capizzi, F. Martelli, S. Rubini, G. Bisognin, and M. Berti, Hydrogen diffusion in $GaAs_{1-x}N_x$, Phys. Rev. B **80**, 195206 (2009).

[33] M. Felici, A. Polimeni, G. Salviati, L. Lazzarini, N. Armani, F. Masia, M. Capizzi, F. Martelli, M. Lazzarino, G. Bais, M. Piccin, S. Rubini, and A. Franciosi, In-plane bandgap engineering by modulated hydrogenation of dilute nitride semiconductors, Adv. Mater. **18**, 1993 (2006).

[34] R. Trotta, A. Polimeni, and M. Capizzi, Hydrogen incorporation in III-N-V semiconductors: From macroscopic to nanometer control of the materials' physical properties, Adv. Funct. Mater. **22**, 1782 (2012).

[35] R. Trotta, A. Polimeni, F. Martelli, G. Pettinari, M. Capizzi, L. Felisari, S. Rubini, M. Francardi, A. Gerardino, P. C. M. Christianen, and J. C. Maan, Fabrication of site-controlled quantum dots by spatially selective incorporation of hydrogen in Ga(AsN)/GaAs heterostructures, Adv. Mater. **23**, 2706 (2011).

[36] S. Birindelli, M. Felici, J. S. Wildmann, A. Polimeni, M. Capizzi, A. Gerardino, S. Rubini, F. Martelli, A. Rastelli, and R. Trotta, Single photons on demand from novel site-controlled GaAsN/GaAsN:H quantum dots, Nano Lett. **14**, 1275 (2014).

[37] P. Gallo, M. Felici, B. Dwir, K. A. Atlasov, K. F. Karlsson, A. Rudra, A. Mohan, G. Biasiol, L. Sorba, and E. Kapon, Integration of site-controlled pyramidal quantum dots and photonic crystal membrane cavities, Appl. Phys. Lett. **92**, 263101 (2008).

[38] M. Calic, P. Gallo, M. Felici, K. A. Atlasov, B. Dwir, A. Rudra, G. Biasiol, L. Sorba, G. Tarel, V. Savona, and E. Kapon, Phonon-mediated coupling of InGaAs/GaAs quantum-dot excitons to photonic crystal cavities, Phys. Rev. Lett. **106**, 227402 (2011).

[39] G. Bisognin, D. De Salvador, A. V. Drigo, E. Napolitani, A. Sambo, M. Berti, A. Polimeni, M. Felici, M. Capizzi,

M. Guengerich, and P. J. Klar, Hydrogen-nitrogen complexes in dilute nitride alloys: Origin of the compressive lattice strain, Appl. Phys. Lett. **89**, 061904 (2006).

[40] G. Bisognin, D. De Salvador, E. Napolitani, M. Berti, A. Polimeni, M. Capizzi, S. Rubini, F. Martelli, and A. Franciosi, High-resolution x-ray diffraction in situ study of very small complexes: The case of hydrogenated dilute nitrides, J. Appl. Crystallogr. **41**, 366 (2008).

[41] M. H. Du, S. Limpijumnong, and S. B. Zhang, Hydrogen pairs and local vibrational frequencies in H-irradiated $GaAs_{1-y}N_y$, Phys. Rev. B **72**, 073202 (2005).

[42] G. Bisognin, D. De Salvador, C. Mattevi, M. Berti, A. V. Drigo, G. Ciatto, L. Grenouillet, P. Duvaut, P. Gilet, and H. Mariette, Determination of lattice parameter and of N lattice location in $In_xGa_{1-x}N_yAs_{1-y}$/GaAs and GaN_yAs_{1-y}/GaAs epilayers, J. Appl. Phys. **95**, 48 (2004).

[43] S. Hein, P. Podemski, G. Sęk, J. Misiewicz, P. Ridha, A. Fiore, G. Patriarche, S. Hoefling, and A. Forchel, Orientation dependent emission properties of columnar quantum dash laser structures, Appl. Phys. Lett. **94**, 241113 (2009).

[44] A. Mohan, P. Gallo, M. Felici, B. Dwir, A. Rudra, J. Faist, and E. Kapon, Engineering conduction and valence band states in site-controlled pyramidal quantum dots, Appl. Phys. Lett. **98**, 253102 (2011).

[45] R. Oulton, B. D. Jones, S. Lam, A. R. A. Chalcraft, D. Szymanski, D. O'Brien, T. F. Krauss, D. Sanvitto, A. M. Fox, D. M. Whittaker, M. Hopkinson, and M. S. Skolnick, Polarized quantum dot emission from photonic crystal nanocavities studied under mode-resonant enhanced excitation, Opt. Express **15**, 17221 (2007).

[46] T. Akiyama, M. Ekawa, M. Sugawara, K. Kawaguchi, H. Sudo, A. Kuramata, H. Ebe, and Y. Arakawa, An ultrawide-band semiconductor optical amplifier having an extremely high penalty-free output power of 23 dBm achieved with quantum dots, IEEE Photonics Technol. Lett. **17**, 1614 (2005).

[47] J. T. Borenstein, J. W. Corbett, and S. J. Pearton, Kinetic-model for hydrogen reactions in boron-doped silicon, J. Appl. Phys. **73**, 2751 (1993).

[48] R. Trotta, A. Polimeni, M. Capizzi, F. Martelli, S. Rubini, M. Francardi, A. Gerardino, and L. Mariucci, Light polarization control in strain-engineered GaAsN/GaAsN:H heterostructures, Appl. Phys. Lett. **94**, 261905 (2009).

[49] R. Trotta, L. Cavigli, L. Felisari, A. Polimeni, A. Vinattieri, M. Gurioli, M. Capizzi, F. Martelli, S. Rubini, L. Mariucci, M. Francardi, and A. Gerardino, Quantum confinement effects in hydrogen-intercalated $Ga_{1-x}As_xN_x - GaAs_{1-x}N_x$:H planar heterostructures investigated by photoluminescence spectroscopy, Phys. Rev. B **81**, 235327 (2010).

[50] M. Felici, A. Polimeni, E. Tartaglini, A. Notargiacomo, M. De Luca, R. Carron, D. Fekete, B. Dwir, A. Rudra, M. Capizzi, and E. Kapon, Reduced temperature sensitivity of the polarization properties of hydrogenated InGaAsN V-groove quantum wires, Appl. Phys. Lett. **101**, 151114 (2012).

[51] G. L. Bir and G. E. Pikus, *Symmetry and Strain-Induced Effects in Semiconductors* (John Wiley and Sons, New York, 1974).

[52] I. Vurgaftman, J. Meyer, and L. Ram-Mohan, Band parameters for III-V compound semiconductors and their alloys, J. Appl. Phys. **89**, 5815 (2001).

[53] S. Kumar, E. Zallo, Y. H. Liao, P. Y. Lin, R. Trotta, P. Atkinson, J. D. Plumhof, F. Ding, B. D. Gerardot, S. J. Cheng, A. Rastelli, and O. G. Schmidt, Anomalous anti-crossing of neutral exciton states in GaAs/AlGaAs quantum dots, Phys. Rev. B **89**, 115309 (2014).

[54] E. V. K. Rao, A. Ougazzaden, Y. Le Bellego, and M. Juhel, Optical properties of low band gap $GaAs_{1-x}N_x$ layers: Influence of post-growth treatments, Appl. Phys. Lett. **72**, 1409 (1998).

[55] A. Polimeni, M. Bissiri, A. Augieri, G. B. Hoger von Högersthal, M. Capizzi, D. Gollub, M. Fischer, M. Reinhardt, and A. Forchel, Reduced temperature dependence of the band gap in $GaAs_{1-y}N_y$ investigated with photoluminescence, Phys. Rev. B **65**, 235325 (2002).

[56] A. Amore Bonapasta, F. Filippone, and G. Mattioli, H-induced dangling bonds in H-isoelectronic-impurity complexes formed in $GaAs_{1-y}N_y$ alloys, Phys. Rev. Lett. **98**, 206403 (2007).

[57] Y. Kohmura, K. Sawada, and T. Ishikawa, Berry-phase translation of x rays by a deformed crystal, Phys. Rev. Lett. **104**, 244801 (2010).

[58] Marco Felici, Giorgio Pettinari, Simone Birindelli, Michela Fratini, Antonio Polimeni, Luisa Barba, Annamaria Gerardino, Luca Businaro, Andrea Notargiacomo, Alessia Cedola, Gaetano Campi, Silvia Rubini, Faustino Martelli, and Mario Capizzi, Berry-phase translation effect in strain-engineered hydrogenated dilute nitrides: A novel approach to x-ray photonics (to be published).